Int. J. Heat Mass Transfer. Vol. 31, No. 7, pp. 1409–1421, 1988
Printed in Great Britain

0017-9310/88 $3.00 + 0.00

Two-dimensional heat transfer study on the keyhole plasma arc welding process

Y. F. HSU and B. RUBINSKY
Department of Mechanical Engineering, University of California, Berkeley, CA 94720, U.S.A.

(*Received* 9 *December* 1986 *and in final form* 3 *December* 1987)

Abstract—This paper presents a two-dimensional, quasi-stationary finite element numerical model to study the fluid flow and the heat transfer phenomena which occur during constant travel speed, keyhole plasma arc welding of metal plates. A Newton–Raphson iteration procedure was developed in this model to accurately identify the solid–liquid interface location during welding. The finite element method was applied to the study of a typical keyhole welding process of an AISI 304 stainless steel plate. The results show that the method can be used to predict the shape of the welding pool as a function of welding parameters and that the widths of both the fusion zone and the heat effected zone decrease as the welding speed increases while the power required for welding increases with an increase in welding speed.

INTRODUCTION

PLASMA arc welding (PAW) is a joining process in which a constricting plasma arc is used as the concentrated energy source to melt and then fuse two metal pieces together [1, 2]. The plasma arc is a high-temperature, partially ionized gas stream produced by forcing an inert gas to flow through an electric field. This electric field is set up between a tungsten electrode (cathode) inside the welding torch and the workpieces (anode) to be welded. The arc temperature and thermal ionization are maintained, by the resistance heating effect of the current flowing through the plasma arc. The arc is further columnized by passing it through a constricting orifice on its way from the welding torch toward the workpiece. In this way, a high-temperature (10 000–20 000 K), high-velocity (300–2000 m s^{-1}) plasma arc is generated for metal processing [3].

As the plasma arc impinges on the area where two workpieces are to be joined, it can melt material and create a molten liquid pool. Because of its high velocity and the associate momentum, the arc can penetrate through the molten liquid pool and form a hole at the point of welding usually referred to as a 'keyhole'. Moving the welding torch and the associated keyhole will cause the flow of the molten metal surrounding the keyhole to the rear region where it resolidifies to form a weld bead.

The PAW process has a number of advantages over other arc welding processes such as gas tungsten arc welding (GTAW). Plasma arc welding can be used for welding thicker pieces with a single pass, does not require preparation of joints, and therefore can be used without filler material. The keyhole mode of welding is the primary attribute of PAW that makes it so attractive.

Keyholes are also formed in electron beam welding (EBW) and laser welding. However, the mechanism of keyhole formation in these processes is different from that in the PAW process. In PAW the keyhole is produced and maintained mainly by the pressure of the penetrating arc rather than by the pressure of the evaporating workpiece material as in EBW and laser welding. Thus, the keyhole appearing in the PAW process is much wider than those produced by either EBW or laser welding processes and has a circular shape [5]. Although all these keyhole welding processes can generate high quality welds, the PAW process turns out to be more attractive because of its cost effectiveness [6].

Plasma arc welding is used extensively for different applications such as welding of missile cases, pipes [7], rocket motor cases [8], advanced high performance ship structures [10], the shuttle rocket booster [4, 14] and with different materials such as stainless steel [7, 9], nickel, nickel alloys, titanium [2] and aluminum alloys [4, 13, 14]. Most of the research on PAW is of an experimental nature with the major emphasis on attempts to identify optimal values of welding current, torch travel speed, plasma gas flow rate, arc length [9], torch orifice [12], and plasma polarity [9, 13, 14] for a good weld.

Limited theoretical studies on the thermal and fluid mechanics aspects of the keyhole welding process can be found in the open literature. In an earlier work this process was modelled as a two-dimensional heat conduction problem involving a constantly moving point heat source [18]. By assuming that the problem is quasi-stationary (with respect to a coordinate system which moves with the heat source) and the material properties are invariant with temperature, analytical expressions of the temperature distribution in a plane normal to the torch axis were derived. The size of the welding pool was then assessed from the location of the isotherm at the melting temperature.

NOMENCLATURE

A	coefficient matrix defined in equation (A6)
a	keyhole radius [m]
B, C	coefficient matrices defined in equation (A6)
C_l, C_s	heat capacity of liquid, solid [J kg^{-1} °C^{-1}]
D	coefficient matrix defined in equation (A6)
e_i	temperature mismatch at interfacial node i, $T_{s,i} - T_m$ [°C]
E	vector of temperature mismatch
$\mathbf{F}_x, \mathbf{F}_y$	vectors of surface force at element boundary, defined in equation (A6)
G	coefficient matrix defined in equation (A6)
h	surface heat transfer coefficient [W m^{-2} °C^{-1}]
h_{ls}	heat of fusion [kJ kg^{-1}]
H	coefficient matrix defined in equation (A6)
J	Jacobian matrix defined in equation (A6)
k_l, k_s	thermal conductivity of liquid, solid [W m^{-1} °C^{-1}]
M	total number of nodes on the solid–liquid interface
M	coefficient matrix defined in equation (A6)
n	normal direction
N	coefficient matrix defined in equation (A6)
P	pressure in the liquid region [N m^{-2}]
$\mathbf{Q}_l, \mathbf{Q}_s$	vectors of heat flux across the element boundary, defined in equations (A6)
r	radial coordinate, defined in Fig. 2
r_i	radial distance between the coordinate origin and the interfacial node [m]
R	vector of interfacial nodal distance
T_b	boiling temperature [°C]
T_l	temperature difference between the liquid and the ambient [°C]
T_m	melting temperature [°C]
T_s	temperature difference between the solid and the ambient [°C]
T_∞	ambient temperature [°C]
U	welding speed [m s^{-1}]
u, v	liquid velocity in x-, y-direction [m s^{-1}]
v_r, v_θ	liquid velocity in r-, θ-direction [m s^{-1}]
w	fusion zone width [m]
x	coordinate axis along the welding path, defined in Fig. 1
y	coordinate axis normal to the welding path, defined in Fig. 1
z	plate thickness [m].

Greek symbols

θ	angular coordinate, defined in Fig. 2
μ	liquid viscosity [kg m^{-1} s^{-1}]
ρ	material density [kg m^{-3}]
ϕ_i, ψ_i	interpolation functions used in the finite element formulation
$\delta\Omega_1$	plasma arc–liquid interface
$\delta\Omega_2$	solid–liquid interface.

Subscripts

i, j	index of nodes
l, s	liquid, solid.

Superscripts

k	iteration step index
T	transpose of matrix
-1	inverse of matrix.

Later, this model was modified by Malmuth [19] who incorporated the latent heat effect into the formulation.

Klemens [20] derived expressions which relate the shape of the molten liquid pool to the welding parameters by assuming that the keyhole is a vertical cylinder with a known inner radius. The flow pattern in the liquid pool and the temperature distribution in both the solid and liquid regions, however, were not solved in his analysis.

Mazumder and Steen [21] proposed another model to study the heat transfer of the laser welding process. For calculational purposes, they considered the keyhole region as part of the workpiece, but at a fictitiously high temperature (above the boiling temperature as calculated from the model). Thermal energy was then assumed to transfer from this region into the liquid pool via heat conduction. The temperature dependence of the material properties and the heat of fusion were neglected. With these simplifications, the temperature distribution in the workpiece was numerically calculated.

Dowden *et al.* [22] analytically solved the flow field and the temperature distribution in the molten liquid surrounding the keyhole during the laser welding process. Since both the keyhole and the solid–liquid interface were assumed circular in this two-dimensional, quasi-stationary analysis, the results are restricted to low welding speed conditions.

Recently, Wei and Giedt [23] reported a numerical study of the liquid flow around a cavity produced by an electron beam. Assuming a given shape of the

solid–liquid interface and heat flux conditions on this interface they have calculated the thickness of the liquid layer around the cavity and the temperature on the liquid–cavity interface. A parametric study was performed to assess the effects of various welding parameters on the liquid metal flow.

This paper presents a two-dimensional analysis of the heat transfer and fluid flow during keyhole plasma arc welding. A finite element technique was employed to perform the numerical calculations. The study presents a new numerical procedure using a Newton–Raphson iteration method to accurately identify the solid–liquid interface location as part of the solution to the problem. This novel numerical method was applied to the study of the welding process in a plate made of AISI 304 stainless steel. The liquid motion in the weld pool, the heat transfer in both solid and liquid regions and the shape of the weld pool were determined as a function of the keyhole diameter and the welding velocity.

ANALYSIS

Physical model

Shown in Fig. 1 is a schematic illustration of the keyhole PAW process analyzed in this work. The figure shows the plasma arc penetrating through the keyhole, the liquid metal weld pool surrounding the keyhole and the resolidification of the liquid metal in the rear region of the weld pool which creates the fusion zone. This study is concerned with the heat transfer and fluid flow during the steady state stage of the plasma welding process, in which the welding torch moves with a constant velocity U, and the fluid flow velocities and temperature distributions have reached steady state with respect to a coordinate system moving with the plasma arc. Therefore, the process can be modelled as a quasi-stationary problem in a frame of reference moving with the plasma arc.

Several simplifying assumptions were made to facilitate a solution to this problem. The simplifications were imposed primarily by the limited information in the technical literature on the heat transfer and fluid flow from plasma jets in the keyhole welding mode.

(1) The temperature variation in the metal plate in the axial direction (the axis of the plasma jet, z) was assumed negligibly small relative to the temperature variation in the radial direction and the problem was treated using a fin like formulation in the radial direction. This assumption is justified by the small Biot number based on the metal plate thickness.

(2) The liquid flow in the molten pool is assumed two-dimensional in the radial and angular directions. This assumption was also made in the other studies mentioned in the Introduction. Although the accuracy of this assumption is questionable and has been employed in this work primarily to facilitate a first solution to the problem it can be justified to some extent from experimental observation. Experiments show that in the liquid puddle during welding, in the axial direction (the axis of the plasma jet), the shear forces caused by the plasma jet and the gravity which tend to detach the liquid droplet are counteracted only by the rather weak surface tension forces. Consequently the forces in the axial direction must be of the order of magnitude of the surface tension forces and therefore very small.

(3) Experimental results show that the keyhole that forms during plasma welding is circular [5, 6] probably because of the effect of surface tension. Therefore, in this study the shape of the keyhole will be assumed circular.

(4) The temperature at the keyhole surface is assumed to be the boiling temperature of the metal. This assumption implies some metal vaporization at the plasma–liquid interface which is neglected in this work.

(5) The effective heat transfer coefficient used in calculating the heat loss from the plate surfaces to the surroundings is assumed constant.

(6) The molten liquid is assumed to be Newtonian and incompressible.

(7) Homogeneous, isotropic but temperature-dependent properties are assumed in the solid region.

(8) Homogeneous, isotropic and temperature-independent properties are assumed in the liquid region.

With the above assumptions, the fluid flow and the heat transfer in the liquid pool can be modelled by the following two-dimensional, quasi-stationary equations in a frame of reference moving with the plasma jet:

continuity

$$\frac{\partial u}{\partial x}+\frac{\partial v}{\partial y}=0; \tag{1}$$

momentum in the x-direction

$$\rho u\frac{\partial u}{\partial x}+\rho v\frac{\partial u}{\partial y}-\frac{\partial}{\partial x}\left[-p+2\mu\frac{\partial u}{\partial x}\right]-\frac{\partial}{\partial y}\left[\mu\left(\frac{\partial u}{\partial y}+\frac{\partial v}{\partial x}\right)\right]=0; \tag{2}$$

momentum in the y-direction

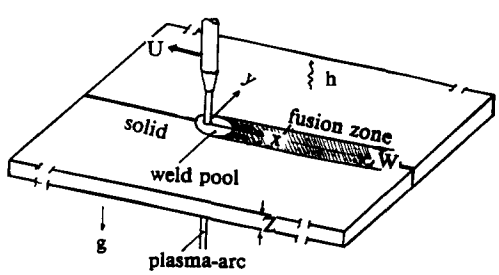

FIG. 1. Keyhole PAW on flat metal plate.

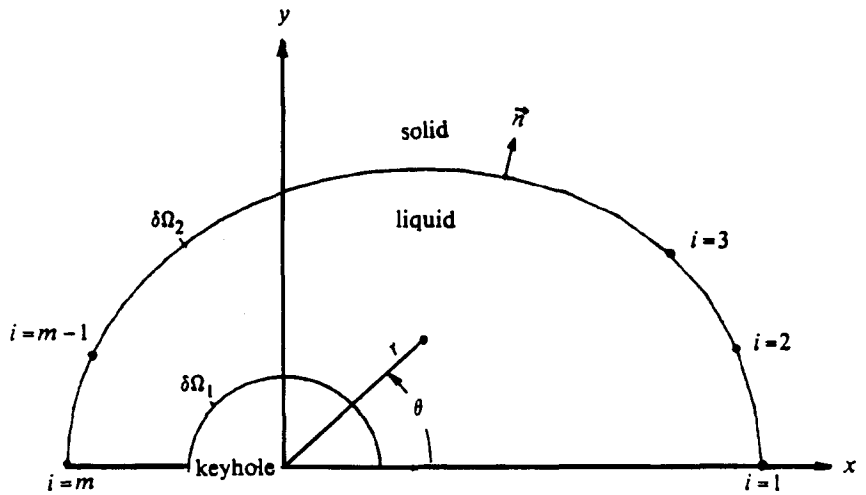

FIG. 2. Coordinate systems defined in molten liquid region.

$$\rho u\frac{\partial v}{\partial x}+\rho v\frac{\partial u}{\partial y}-\frac{\partial}{\partial x}\left[\mu\left(\frac{\partial v}{\partial x}+\frac{\partial u}{\partial y}\right)\right]-\frac{\partial}{\partial y}\left[-p+2\mu\frac{\partial v}{\partial y}\right]=0; \quad (3)$$

energy

$$\rho c_l u\frac{\partial T_l}{\partial x}+\rho c_l v\frac{\partial T_l}{\partial y}-\frac{\partial}{\partial x}\left(k_l\frac{\partial T_l}{\partial x}\right)-\frac{\partial}{\partial y}\left(k_l\frac{\partial T_l}{\partial y}\right)+\frac{2h}{z}T_l=0; \quad (4)$$

where x and y are the axes of the coordinate system defined in Fig. 2; u and v are the liquid velocity components in the x- and y-directions; T_l is defined as the temperature difference between the liquid and the environment which is assumed at a constant value T_∞; h is the effective heat transfer coefficient associated with the surface heat loss; z is the metal plate thickness; p is the pressure in the liquid region.

The heat transfer in the solid region is governed by the following energy equation:

$$\rho c_s U\frac{\partial T_s}{\partial x}-\frac{\partial}{\partial x}\left(k_s\frac{\partial T_s}{\partial x}\right)-\frac{\partial}{\partial y}\left(k_s\frac{\partial T_s}{\partial y}\right)+\frac{2h}{z}T_s=0 \quad (5)$$

where T_s is the temperature difference between the solid temperature and T_∞.

At the centerline (welding path) of the workpiece, the tangential shear stress, the velocity component, and the temperature gradient in the y-direction are all zero due to the symmetry condition. Therefore

$$\frac{\partial u}{\partial y}=0; \quad v=0; \quad \frac{\partial T_l}{\partial y}=0; \quad \frac{\partial T_s}{\partial y}=0; \quad \text{at } y=0. \quad (6)$$

Assuming an infinite plate in the x- and y-direction, far away from the plasma arc and the molten liquid pool, the solid material will remain at the environmental temperature. Thus

$$T_s=0; \quad \text{as } y\to\infty \quad \text{or} \quad x\to\pm\infty. \quad (7)$$

Because the liquid metal cannot flow across the keyhole surface ($\delta\Omega_1$ in Fig. 2), its velocity component in the local normal direction is zero

$$v_r=u\cos\theta+v\sin\theta=0; \quad \text{at } r=(x^2+y^2)^{1/2}=a \quad (8)$$

where r and θ are the polar coordinates defined in Fig. 2; a is the known keyhole radius.

The tangential shear stress of the liquid at the keyhole surface is also zero because the plasma arc cannot resist the sideflow of the liquid metal. This boundary condition can be simplified to take the form

$$\frac{\partial}{\partial r}\left(\frac{v_\theta}{r}\right)=0; \quad \text{at } r=a. \quad (9)$$

According to the initial assumption, the liquid temperature at the keyhole surface is the boiling temperature. Thus

$$T_s=T_b-T_\infty; \quad \text{at } r=a \quad (10)$$

where T_∞ is the constant environment temperature.

On the solid–liquid interface ($\delta\Omega_2$ in Fig. 2), the no-slip condition and the local energy balance lead to the following equations:

$$u=U; \quad \text{on } \delta\Omega_2 \quad (11)$$

$$v=0; \quad \text{on } \delta\Omega_2 \quad (12)$$

$$T_l=T_s=T_m-T_\infty; \quad \text{on } \delta\Omega_2 \quad (13)$$

$$-k_s\frac{\partial T_s}{\partial n}=-k_l\frac{\partial T_l}{\partial n}+\rho U h_{sl}\cos\theta_n; \quad \text{on } \delta\Omega_2 \quad (14)$$

where T_m is the melting temperature of the material; h_{sl} is the heat of fusion; θ_n is the angle between the x-

axis and the local normal to the solid–liquid interface.

Equations (1)–(5) with boundary conditions (6)–(14) form a complete set for the determination of the velocity and temperature fields in the liquid and temperature field in the solid. Because the workpiece is symmetric with respect to the centerline, only one half of the x–y plane is considered in the calculations.

Finite element formulations

In the present numerical study the reduction of the continuum problem to a discrete form is accomplished by employing a Galerkin finite element method [27–29]. This approach divides the geometric domain of interest into a number of isoparametric elements with specified nodes. Within each element the coordinates and the dependent variables, u, v, P, T, at any location are expressed in terms of pre-determined interpolation functions and the variables at those nodal points. These relationships can be written as follows:

$$\begin{aligned} x &= \sum_{i=1}^{N} \phi_i x_i, \quad y = \sum_{i=1}^{N} \phi_i y_i \\ u &= \sum_{i=1}^{N} \phi_i u_i, \quad v = \sum_{i=1}^{N} \phi_i u_i \\ P &= \sum_{i=1}^{N} \psi_i P_i, \quad T = \sum_{i=1}^{N} \phi_i T_i \end{aligned} \tag{15}$$

where ϕ_i and ψ_i are the interpolation functions; x_i and y_i are the coordinates at the ith node; u_i, v_i, P_i and T_i are the unknown dependent variables at the ith node; N nodes are assumed to be associated with each element. By introducing the above approximations into equations (1)–(5) and applying the Galerkin weighted residual procedure to the resultant equations, a set of matrix equations, which represent the discrete form of the continuum equations, can be derived for each element:

continuity

$$\mathbf{B}^{\mathrm{T}}\mathbf{u} + \mathbf{C}^{\mathrm{T}}\mathbf{v} = \mathbf{0}; \tag{16}$$

x-momentum

$$\mathbf{Au} + \mathbf{BP} + \mathbf{Du} + \mathbf{Gv} = \mathbf{F}_x; \tag{17}$$

y-momentum

$$\mathbf{Av} + \mathbf{CP} + \mathbf{G}^{\mathrm{T}}\mathbf{u} + \mathbf{MV} = \mathbf{F}_y; \tag{18}$$

energy in liquid

$$\mathbf{NT}_{\mathrm{l}} = \mathbf{Q}_{\mathrm{l}}; \tag{19}$$

energy in solid

$$\mathbf{HT}_{\mathrm{s}} = \mathbf{Q}_{\mathrm{s}}; \tag{20}$$

where $\mathbf{u}$ and $\mathbf{v}$ are vectors of the velocities at nodal points; $\mathbf{P}$ is the vector of nodal pressure; $\mathbf{T}_{\mathrm{l}}$ and $\mathbf{T}_{\mathrm{s}}$ are vectors of nodal temperatures in liquid and solid region; $\mathbf{B}$ and $\mathbf{C}$ matrices represent the incompressibility constraint; $\mathbf{A}$ matrix represents the liquid inertia term in the momentum equation; $\mathbf{D}$, $\mathbf{G}$ and $\mathbf{M}$ matrices represent the diffusion of momentum; $\mathbf{N}$ and $\mathbf{H}$ matrices represent the combined effects of both convection and diffusion of the thermal energy; $\mathbf{F}_x$ and $\mathbf{F}_y$ are vectors of surface forces applied at the element boundary; $\mathbf{Q}_{\mathrm{l}}$ and $\mathbf{Q}_{\mathrm{s}}$ are vectors of surface heat flux across the element boundary. A detailed finite element formulation of these matrices is listed in the Appendix.

Equations (15)–(20) are derived for a single finite element. By assembling the matrix equations over all the elements, a system of matrix equations which govern the fluid flow and heat transfer in the workpiece is obtained. The nodal point unknowns in the vectors of $\mathbf{u}$, $\mathbf{v}$, $\mathbf{P}$, $\mathbf{T}_{\mathrm{l}}$ and $\mathbf{T}_{\mathrm{s}}$ can then be solved after introducing the boundary conditions, equations (6)–(14), into these matrix equations.

The type of element used in this work is the nine node quadrilateral element with 31 degrees of freedom. The element boundary shape, velocity and temperature fields within each element are approximated using quadratic functions while the interpolation function for pressure is linear and based on the value of the pressure at the corner nodes. This careful choice of the degrees of interpolation functions, i.e. the interpolation function for pressure is one degree less than that for velocity, was made for the consistency of the approximation [28], and is necessary to assure good results.

Solution procedure

A straightforward solution of the finite element equations is not possible because of the unknown location of the solid–liquid interface. In this paper we have developed a Newton–Raphson iteration procedure to accurately identify the solid–liquid interface. This procedure is essentially a prediction–correction method which locates the solid–liquid interface position such that the interfacial thermal conditions, equations (13) and (14), can be both satisfied. A description of the iterative procedure follows.

The iterative procedure is started by setting up a group of nodes on a guessed interface location. These nodes are spaced equally along the angular, θ, direction while the radial distance, r_i ($i = 1, 2, \ldots, m$; m is the total number of nodes on the guessed interface location) from the coordinate origin to the nodes is guessed in the first iteration and then determined through the Newton–Raphson iterative procedure.

First, the flow and temperature fields are determined in the liquid region from the solution of equations (16)–(19) with boundary condition (13). The heat flux on the interface, in the liquid region, is obtained as part of the solution. This heat flux is introduced into equation (14) which then serves as a boundary condition for the solution of the energy equation in the solid region, equation (20). Since the interface location used in this analysis is just a guess, the temperature on the solid–liquid interface obtained from this calculation may be different from the melting temperature, i.e. boundary condition (13) is not satisfied in the solid region.

The difference between the temperature calculated on each node, i, on the interface and the melting temperature is e_i where

$$e_i(r_1, r_2, \ldots, r_m) = T_{s,i} - T_m; \quad i = 1, 2, \ldots, m. \tag{21}$$

The objective of the Newton–Raphson iterative procedure then becomes the minimization of e_i's by properly adjusting the r_i's. Let $\mathbf{E}$ and $\mathbf{R}$ be the vectors of nodal surface temperature difference and interface nodal distance. The following formula is used to update the prediction on $\mathbf{R}$ using the values of $\mathbf{E}$ resulting from the previous prediction

$$\mathbf{R}^{k+1} = \mathbf{R}^k - [\mathbf{J}^k]^{-1}\mathbf{E}^k \tag{22}$$

where the superscript k stands for the iteration number. The element at the ith row, jth column of the Jacobian matrix, $J^k_{i,j}$, is given by

$$J^k_{i,j} = \frac{\partial e^k_i}{\partial r^k_j} \tag{23}$$

or in a numerical form

$$J^k_{i,j} \approx \frac{e^k_i - e^{k-1}_i}{r^k_j - r^{k-1}_j}. \tag{24}$$

In the solution, during each iteration, a new finite element mesh is automatically generated based on the updated location of the solid–liquid interface. Then the temperatures and fluid flow are calculated and a new vector $\mathbf{E}$ generated. This iteration procedure is repeated until the following convergence criterion is met:

$$\left(\frac{\mathbf{E}^T \cdot \mathbf{E}}{m}\right)^{1/2} = 0.002 T_m. \tag{25}$$

RESULTS AND DISCUSSION

The numerical method was used to investigate the heat transfer and fluid flow phenomena during a keyhole PAW process on a 12.7 mm thick stainless steel plate. This study assumed a constant heat transfer coefficient of 20 W m^{-2} K^{-1} between the workpiece surface and the surroundings, which is at a constant temperature of 30°C. Based on these values and the stainless steel properties (Table 1), the Biot number associated with the heat conduction in the plate is found to be less than 0.01. Therefore, the two-dimensional heat transfer model which assumes uniform temperature across the plate thickness is reasonable. The analysis was performed for a keyhole with a radius of 2 mm, which is typical of the PAW process [13]. It is expected that the temperature gradients near the keyhole are larger than those far away from the keyhole. Thus, a finite element mesh of expanding spacing in the radial direction, with finer spacing near the keyhole and coarser spacing far away from it, was used to reduce computer time. A mesh of 360 nodes was used for the solution of the problem.

Table 1. Thermal properties of AISI 304 stainless steel

Temperature	Thermal conductivity (W m^{-1} °C^{-1})	Heat capacity (J kg^{-1} °C^{-1})
0	14.3	460.5
20	14.7	473
27	14.9	477.2
77	15.8	498.1
127	16.6	514.9
177	17.5	527.4
227	18.3	540.0
277	19.1	548.8
327	19.8	556.7
377	20.5	565.1
427	21.2	569.3
477	21.9	577.7
527	22.6	581.9
577	23.3	586.0
627	24.0	594.4
677	24.7	602.8
727	25.7	611.2
827	26.7	623.7
927	28.0	640.5
1027	29.3	653.0
1127	30.5	665.3
1227	31.7	682.3
1327	32.7	694.9
1367	33.3	707.4
1427	31.5	812.1
2807	31.5	812.1

Density, 7200 kg m^{-3}; viscosity, 0.00642 kg m^{-1} s^{-1}; melting temperature, 1427°C; boiling temperature, 2807°C; heat of fusion, 265.2 kJ kg^{-1}.

Figures 3 and 4 show the velocity and temperature fields calculated in the liquid region for constant welding speeds of 0.5 and 2.5 mm s^{-1}. These plots clearly show the flow pattern of the molten liquid in the pool. Since the keyhole moves, the weld pool shape and the temperature isotherms are not circular as in the case of a stationary heat source. The elliptical nature of the pool shape is more prominent for the higher welding speed case.

Figures 5 and 6 illustrate the temperature distributions in the solid region at welding speeds of 0.5 and 2.5 mm s^{-1}. Results show that the isotherms in front of the keyhole are closer than those behind the keyhole because of the convective effect of the welding torch movement. It is also important to observe that the width of the heat affected zone in the workpiece is reduced as the welding speed increases.

The temporal variations of the temperature at a fixed point on the welding path ($y = 0$) is shown in Fig. 7. Results reveal that, for the welding process at a higher speed, material is heated up and cools down at a faster rate. These results are useful in understanding the recrystallization process following welding and the fractures caused by thermal stresses. Experiments done in our laboratory clearly indicate that higher welding rates in plasma welding results in fracture of the weld.

Figure 8 depicts the sizes of the weld pool as a function of welding speed. Five welding speeds rang-

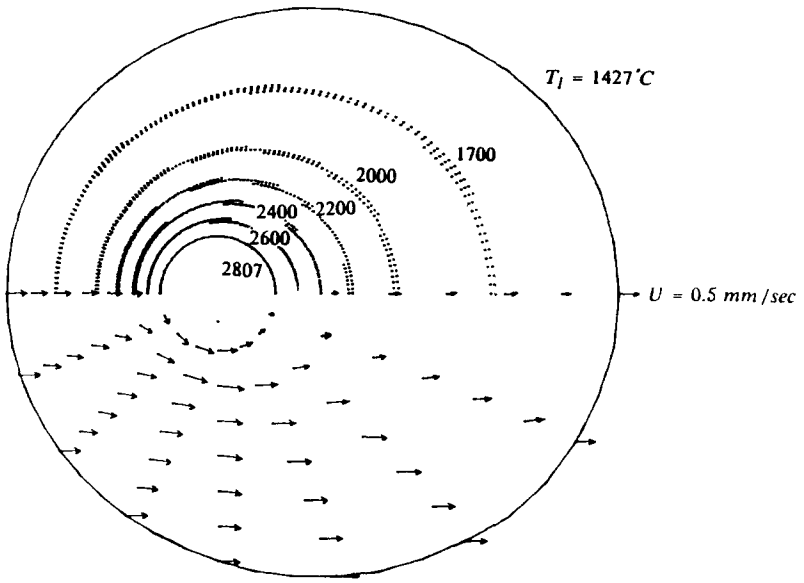

FIG. 3. Velocity and temperature distributions in the liquid region, welding speed = 0.5 mm s^{-1}.

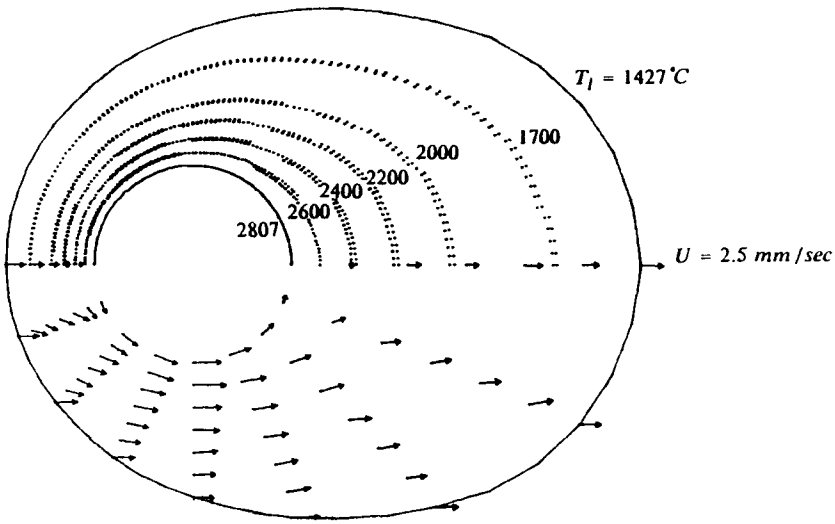

FIG. 4. Velocity and temperature distributions in the liquid region, welding speed = 2.5 mm s^{-1}.

ing from 0.5 to 2.5 mm s^{-1} were considered. It can be seen, that the weld pool at a higher speed is smaller. This implies that a narrower fusion zone may be obtained as the welding speed increases. Figure 9 presents a correlation between the width of the fusion zone and the welding speed. These predictions are consistent with the experimental results in our laboratory which will be published in a forthcoming publication.

Also shown in Fig. 10 is the minimal power requirement for welding per unit plate thickness as a function of welding speed. This power requirement is the heat needed by the workpiece to maintain a constant speed welding process. As revealed in this figure, this power increases, almost linearly, with the welding speeds discussed here. This is caused by the fact that more solid material, per unit time, will be heated up during a process at a higher speed. This data also represents, to the approximations made in this study, the maximum heat that the workpiece can absorb during the welding process. Any additional heat which is transferred from the plasma arc to the workpiece would be used to vaporize the metal. For the case of a welding speed of 2.5 mm s^{-1}, this power requirement is about 2.1 kW. The power input used during a typical PAW process on stainless steel plates was found

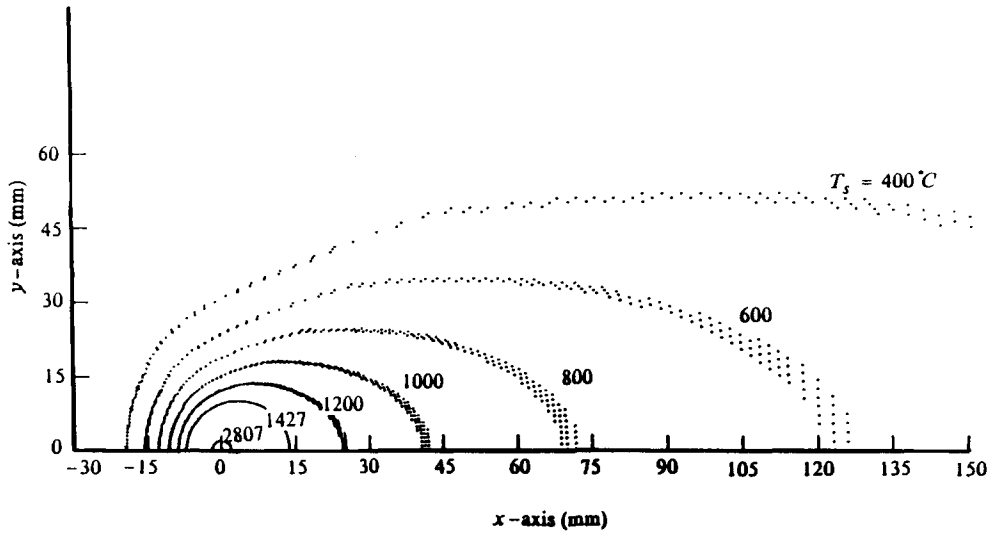

FIG. 5. Temperature distribution in the solid region, welding speed = 0.5 mm s^{-1}.

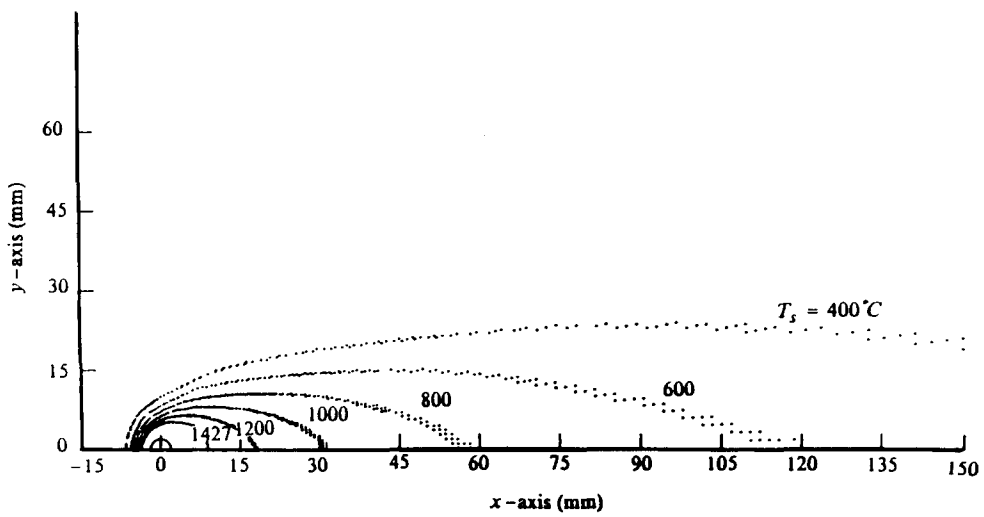

FIG. 6. Temperature distribution in the solid region, welding speed = 2.5 mm s^{-1}.

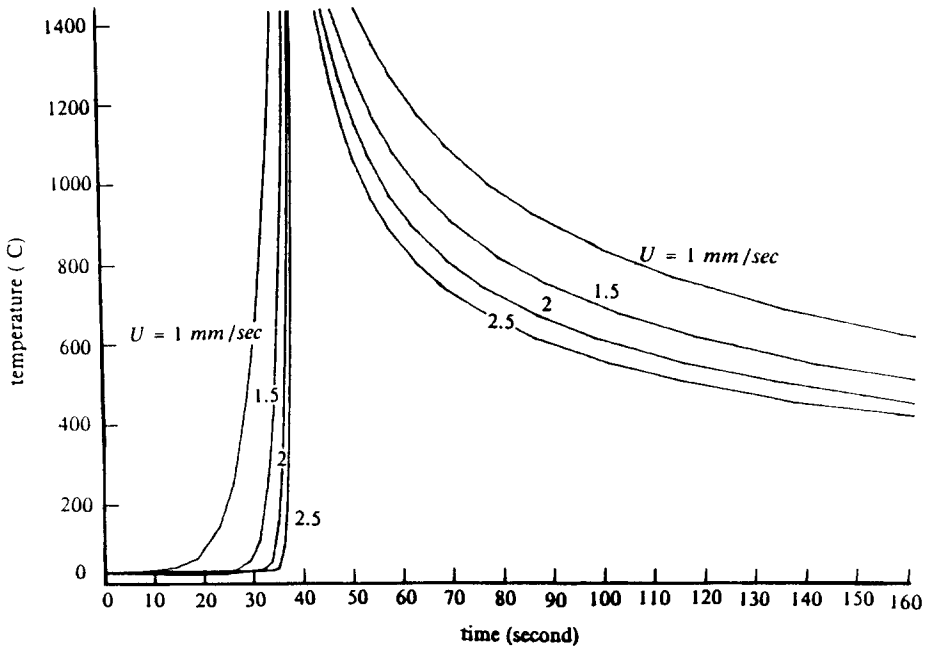

FIG. 7. Temperature history of a fixed point on the welding path.

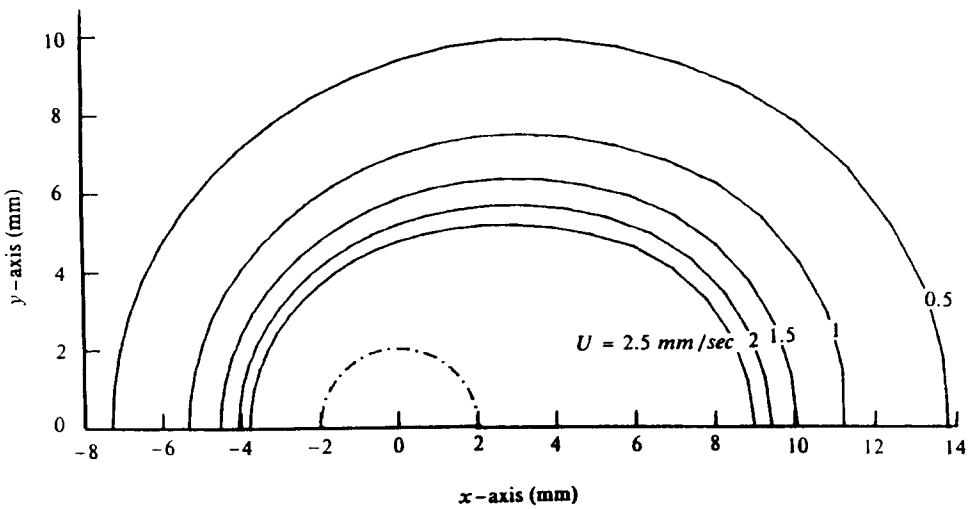

FIG. 8. Solid–liquid interfaces at different welding speeds.

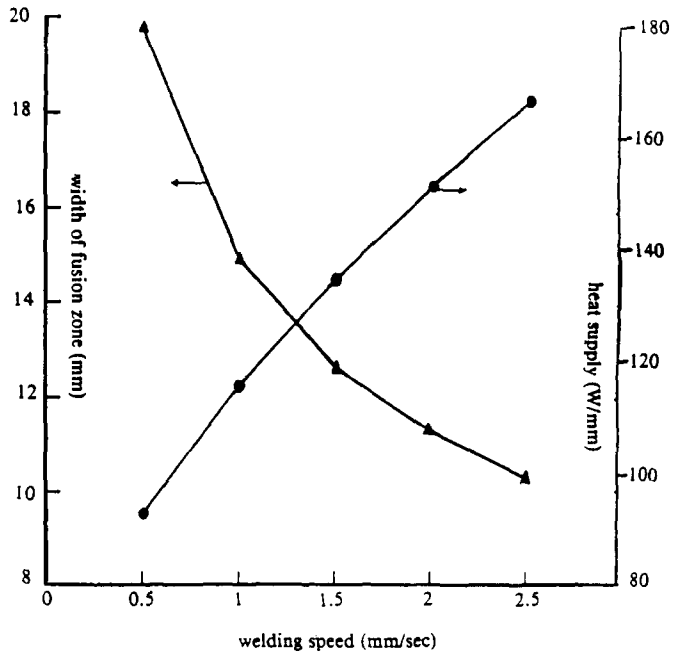

FIG. 9. Fusion zone width and minimal heat supply vs welding speed.

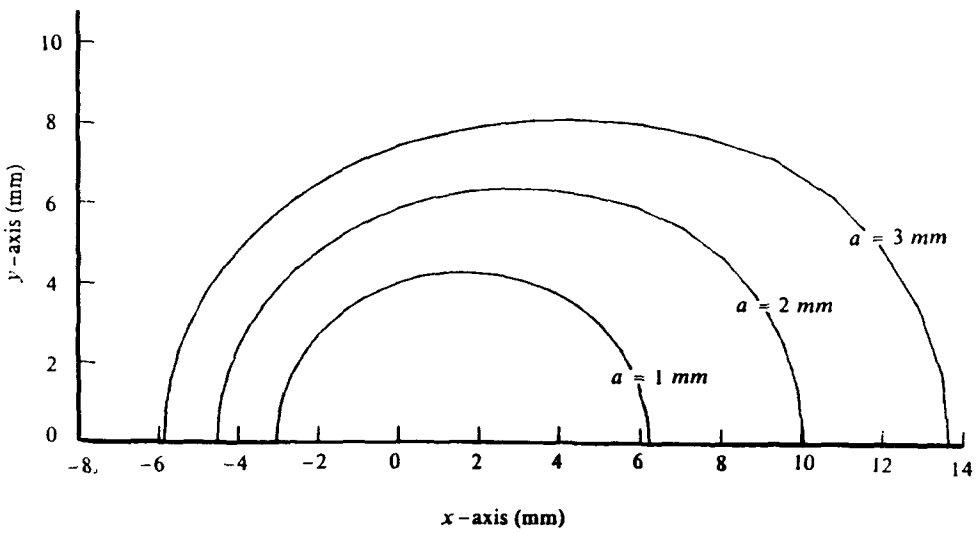

FIG. 10. Solid–liquid interfaces calculated at different keyhole sizes, welding speed = 1.5 mm s^{-1}.

experimentally to be in the range of 4–10 kW [24]. By assuming a typical heat transfer efficiency of 65% for the process [11], the power required for PAW of a 12.7 mm plate with a keyhole of 2 mm will vary, according to Fig. 9, between 2.6 and 6.5 kW. This result compares favorably with the experimental results and may show that some metal vaporization would occur during the PAW process.

The effect of keyhole size on the weld pool size is shown in Fig. 10. Three keyhole radii of 1, 2 and 3 mm were considered in this study. This plot shows that the weld pool size increases with the keyhole radius. Similarly, the required thermal energy increases with the keyhole radius (see Fig. 9). This result suggests a method to control PAW processes through the control of the plasma jet diameter.

To determine the effects of the thickness of the plate on the solution, Fig. 11 shows the solid–liquid interface evaluated at Biot numbers (hZ/k_s) of 0.008 and 0.08. The welding speed and the keyhole radius assumed in these calculations were 1.5 mm s^{-1} and 2 mm, respectively. It is evident from the small change in the weld pool size that the welding process will not be affected by the thickness of the plate if the Biot

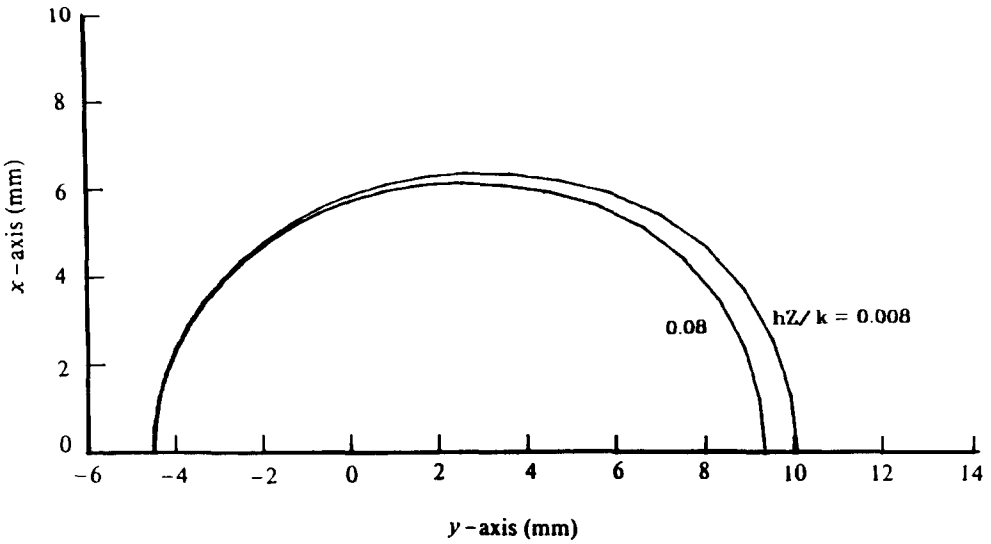

FIG. 11. Solid–liquid interfaces calculated at $h = 20$ and 200 W m^{-2} °C^{-1}.

number is small, and when the boundary conditions on the plasma–liquid interface do not vary in the axial direction.

CONCLUSION

A new finite element numerical method was developed to study the fluid flow and the heat transfer processes during keyhole PAW of metal plates. This model employs a Newton–Raphson iteration procedure, to accurately identify the solid–liquid interface location. A parametric study of the welding of an AISI 304 stainless steel plate indicates the importance of the welding speed and keyhole size on the widths of both the fusion zone and the heat affected zone and on the energy required for welding. A higher welding speed will increase the energy requirement for welding and decrease the width of the heat affected zone, while a large keyhole size will increase both, the width of the heat affected zone and the energy requirement. The results have been found to be qualitatively consistent with the experimental results in the literature.

Acknowledgements—This study was performed with the support of the FMC Corporation, Welding Engineering Group. The authors would like to express their appreciation to Messrs D. Witkowski and K. L. Keck for the suggestion of this topic of research, and the continuous consultations.

REFERENCES

1. R. L. O'Brien, Arc plasma for joining, cutting and surfacing, *WRC Bull.* No. 131, 1–20 (July 1968).
2. Progress in plasma technology, *Weld. Metal Fabric.* 46–50 (February 1970).
3. J. C. Metcalfe and M. B. C. Quigley, Heat transfer in plasma-arc welding, *Weld. J.* **54,** 995–1035 (March 1975).
4. M. Tomsic and S. Barhorst, Keyhole plasma arc welding of aluminum with variable polarity power, *Weld. J.* **63,** 25–32 (February 1984).
5. J. F. Lancaster, *The Physics of Welding*, Chap. 8. Pergamon Press, Oxford (1984).
6. R. E. Regan, Plasma arc welding: state-of-art survey, Boeing Company Report No. D324-11012-1, published as Appendix to: R. L. McCaw, Plasma arc welding of high-performance ship materials, David W. Taylor Naval Ship Research and Development Center, Report No. DTNSRDC/SME-78/34, pp. 19–84 (1977).
7. H. R. Miller and S. P. Filipski, Automated plasma arc welding for aerospace and cryogenic fabrications, *Weld. J.* **45,** 493–501 (June 1966).
8. L. J. Privoznik and H. R. Miller, Evaluation of plasma arc welding for 120 inch diameter rocket motor cases, *Weld. J.* **45,** 717–725 (September 1966).
9. M. J. Tomsic and C. E. Jackson, Energy distribution in keyhole mode plasma arc welds, *Weld. J.* **53,** 109–115 (March 1974).
10. J. C. Metcalfe and M. B. C. Quigley, Keyhole stability in plasma arc welding, *Weld. J.* **54,** 401–404 (November 1975).
11. V. P. Demyantsevich and N. A. Sosnin, Some ways of increasing the efficiency of the plasma arc, *Weld. Prod.* **21**(4), 26–29 (1974).
12. C. B. Shaw, Jr., Effect of orifice geometry in plasma-arc welding of Ti–6Al–4V, *Weld. J.* **59,** 1215–1255 (April 1980).
13. G. Cooper, J. Palermo and J. A. Browning, Recent developments in plasma welding, *Weld. J.* **44,** 268–276 (April 1965).
14. A. C. Nunes, E. O. Bayless, C. S. Jones, P. M. Munafo, A. P. Biddle and W. A. Wilson, Variable polarity plasma arc welding on the space shuttle external tank, *Weld. J.* **63,** 27–35 (September 1984).
15. D. Rosenthal, Mathematical theory of heat distribution during cutting and welding, *Weld. J.* **20,** 2205–2345 (May 1941).
16. P. S. Myers, O. A. Byehana and G. L. Borman, Fundamentals of heat flow in welding, *Weld. Res. Coun. Bull.* No. 123 (July 1967).
17. N. Christensen, V. de L. Davies and K. Gjermundsen, Distribution of temperatures in arc welding, *Br. Weld. J.* **12,** 54–75 (February 1965).

18. D. T. Swift-Hook and A. E. F. Gick, Penetration welding with lasers, *Weld. J.* **52,** 4925–4995 (November 1973).
19. N. D. Malmuth, Temperature field of a moving point source with change of state, *Int. J. Heat Mass Transfer* **19,** 349–354 (1976).
20. P. G. Klemens, Heat balance and flow conditions for electron beam and laser welding, *J. Appl. Phys.* **47,** 2165–2174 (1976).
21. J. Mazumder and W. M. Steen, Heat transfer for CW laser material processing, *J. Appl. Phys.* **51**(2), 941–947 (1980).
22. J. Dowden, M. Davis and P. Kapadia, Some aspects of the fluid dynamics of laser welding, *J. Fluid Mech.* **126,** 123–146 (1983).
23. P. S. Wei and W. H. Giedt, Surface tension gradient-driven flow around an electron beam welding cavity, *Weld. J.* **64,** 2515–2595 (September 1985).
24. S. Kou, T. Kanevsky and S. Fyfitch, Welding thin plates of aluminum alloys—a quantitative heat-flow analysis, *Weld. J.* **61,** 1755–1815 (June 1982).
25. C. Chan, J. Mazumder and M. M. Chen, A two-dimensional transient mode for convection in laser melted pool, *Metall. Trans.* **15A,** 2175–2184 (1984).
26. S. Kou and Y. Le, Three dimensional heat flow and solidification during the autogenous GTA welding of aluminum plates, *Metall. Trans.* **14A,** 2245–2253 (November 1983).
27. D. K. Gartling and E. B. Becker, Finite element analysis of viscous incompressible fluid flow, Part I: basic methodology, *Comp. Meth. Appl. Engng* No. 8, 51–60 (1976).
28. D. K. Gartling, Convective heat transfer analysis by the finite element method, *Comp. Meth. Appl. Mech. Engng* No. 12, 365–382 (1977).
29. J. N. Reddy, *An Introduction to the Finite Element Method*, pp. 280–283. McGraw-Hill, New York (1984).

APPENDIX

Using the Galerkin finite element procedure, the field equations (4-21) through (5) can be transformed into the following elemental matrix equations:

$$\mathbf{B}^T\mathbf{u}+\mathbf{C}^T\mathbf{v}=\mathbf{0} \tag{A1}$$

$$\mathbf{Au}+\mathbf{Bp}+\mathbf{Du}+\mathbf{Gv}=\mathbf{F}_x \tag{A2}$$

$$\mathbf{Av}+\mathbf{Cp}+\mathbf{G}^T\mathbf{u}+\mathbf{Mv}=\mathbf{F}_y \tag{A3}$$

$$\mathbf{NT}_l=\mathbf{Q}_l \tag{A4}$$

$$\mathbf{HT}_s=\mathbf{Q}_s. \tag{A5}$$

The elements at the ith row, jth column of each of the coefficient matrices above are listed as follows:

$$A_{i,j}=\iint_{\Omega_l}\rho\phi\frac{\partial\phi_j}{\partial x}\left(\sum_{k=1}^{N}\phi_k u_k\right)\mathrm{d}x\,\mathrm{d}y+\iint_{\Omega_l}\rho\phi\frac{\partial\phi_j}{\partial y}\left(\sum_{k=1}^{N}\phi_k v_k\right)\mathrm{d}x\,\mathrm{d}y$$

$$B_{i,j}=-\iint_{\Omega_l}\frac{\partial\phi_i}{\partial x}\psi_j\,\mathrm{d}x\,\mathrm{d}y$$

$$C_{i,j}=-\iint_{\Omega_l}\frac{\partial\phi_i}{\partial y}\psi_j\,\mathrm{d}x\,\mathrm{d}y$$

$$D_{i,j}=\iint_{\Omega_l}\mu\left(2\frac{\partial\phi_i}{\partial x}\frac{\partial\phi_j}{\partial x}+\frac{\partial\phi_i}{\partial y}\frac{\partial\phi_j}{\partial y}\right)\mathrm{d}x\,\mathrm{d}y$$

$$G_{i,j}=\iint_{\Omega_l}\mu\frac{\partial\phi_i}{\partial y}\frac{\partial\phi_j}{\partial x}\mathrm{d}x\,\mathrm{d}y$$

$$H_{i,j}=\iint_{\Omega_l}\left(\rho c_s\phi_i\frac{\partial\phi_j}{\partial x}U+k_s\frac{\partial\phi_i}{\partial x}\frac{\partial\phi_j}{\partial x}+k_s\frac{\partial\phi_i}{\partial y}\frac{\partial\phi_j}{\partial y}+\frac{2h}{z}\phi_i\phi_j\right)\mathrm{d}x\,\mathrm{d}y$$

$$M_{i,j}=\iint_{\Omega_l}\mu\left(\frac{\partial\phi_i}{\partial x}\frac{\partial\phi_j}{\partial x}+2\frac{\partial\phi_i}{\partial y}\frac{\partial\phi_j}{\partial y}\right)\mathrm{d}x\,\mathrm{d}y$$

$$N_{i,j}=\iint_{\Omega_l}\rho c_l\phi_i\left[\frac{\partial\phi_j}{\partial x}\left(\sum_{k=1}^{N}\phi_k v_k\right)+\frac{\partial\phi_j}{\partial y}\left(\sum_{k=1}^{N}\phi_k v_k\right)\right]\mathrm{d}x\,\mathrm{d}y+\iint_{\Omega_l}\left(k_l\frac{\partial\phi_i}{\partial x}\frac{\partial\phi_j}{\partial x}+k_l\frac{\partial\phi_i}{\partial y}\frac{\partial\phi_j}{\partial y}+\frac{2h}{z}\phi_i\phi_j\right)\mathrm{d}x\,\mathrm{d}y$$

$$F_{x,i}=\iint_{\delta\Omega_l}\phi_i\left[\left(-p+2\mu\frac{\partial u}{\partial x}\right)n_x+\mu\left(\frac{\partial u}{\partial y}+\frac{\partial v}{\partial x}\right)n_y\right]$$

$$F_{y,i}=\int_{\delta\Omega_l}\phi_i\left[\mu\left(\frac{\partial u}{\partial y}+\frac{\partial v}{\partial x}\right)n_x+\left(-p+2\mu\frac{\partial v}{\partial y}n_y\right)\right]\mathrm{d}\Gamma$$

$$Q_{l,i}=-\int_{\delta\Omega_l}\phi_i\left(-k_l\frac{\partial T_l}{\partial n}\right)\mathrm{d}\Gamma$$

$$Q_{s,i}=-\int_{\delta\Omega_l}\phi_i\left(-k_s\frac{\partial T_s}{\partial n}\right)\mathrm{d}\Gamma. \tag{A6}$$

ETUDE DU TRANSFERT THERMIQUE BIDIMENSIONNEL POUR LE MECANISME DE SOUDAGE PAR PLASMA D'ARC

Résumé—On présente un modèle bidimensionnel, quasi-stationnaire pour étudier numériquement par la méthode des éléments finis l'écoulement fluide et le transfert de chaleur qui se produisent pendant le soudage à vitesse constante de plaques métalliques à l'aide d'un plasma d'arc. On développe une procédure itérative de Newton–Raphson pour identifier avec précision la position de l'interface liquide–solide. Les résultats montrent que la méthode peut être utilisée pour prédire la forme de la zone fondue en fonction des paramètres de soudage. Les étendues de la zone fondue et de la zone chaude diminuent quand la vitesse de soudage augmentent tandis que la puissance nécessaire au soudage augmente lorsque la vitesse de soudage croît.

UNTERSUCHUNG DES ZWEIDIMENSIONALEN WÄRMETRANSPORTS BEIM PLASMA-LICHTBOGENSCHWEISSEN

Zusammenfassung—Die Abhandlung beschreibt ein zweidimensionales quasi-stationäres Finite-Element-Modell zur Untersuchung von Strömung und Wärmeübertragung beim Plasma-Lichtbogen-Schweißen an Metallplatten bei konstanter Vorschub-Geschwindigkeit. Ein Newton–Raphson-Iterationsverfahren wurde entwickelt, um die Lage der Schmelzfront während des Schweißvorgangs möglichst exakt zu bestimmen. Die Finite-Element-Methode wurde dazu verwendet, den typischen Durchschweißprozeß an einer Platte aus rostfreiem Stahl (AISI 304) zu untersuchen. Die Ergebnisse zeigen, daß die Methode zur Bestimmung der Form des Schmelzgebiets als Funktion der Schmelzparameter angewandt werden kann. Die Breite der Schmelzzone und das erhitzte Gebiet werden bei steigender Vorschubgeschwindigkeit kleiner, während die notwendige elektrische Leistung ansteigt.

ИЗУЧЕНИЕ ДВУМЕРНОГО ТЕПЛОПЕРЕНОСА В ПРОЦЕССЕ ПЛАЗМЕННОЙ ДУГОВОЙ СВАРКИ ТИПА «ЛАСТОЧКИН ХВОСТ»

Аннотация—Представлена двумерная квазистационарная численная модель конечных элементов для исследования течения жидкости и явлений теплопереноса, которые имеют место в случае плазменной дуговой сварки металлических пластин типа «ласточкин хвост» с постоянной скоростью. С целью точного определения при сварке границы раздела твердое тепло–жидкость в этой модели был усовершенствован итерационный метод Ньютона–Рафсона. Метод конечных элементов применялся для изучения типичного процесса сварки пластины типа «ласточкин хвост» из нержавеющей стали AISI 304. Результаты показывают, что данный метод может быть использован для расчета формы сварочной ванны в функции параметров сварки и что ширина как зоны плавления, так и зоны термического влияния уменьшается с ростом скорости сварки в то время как потребная мощность увеличивается.